PHYSICAL REVIEW A **78**, 042704 (2008)

Comparative study of electron and positron scattering by H_2: The role of the $^2\Sigma_g^+$ Feshbach resonance

Eliane M. de Oliveira and Marco A. P. Lima
Instituto de Física Gleb Wataghin, Universidade Estadual de Campinas, 13083-970, Campinas, São Paulo, Brazil

Márcio T. do N. Varella
Universidade Federal do ABC, Centro de Ciências Naturais e Humanas, Rua Santa Adélia, 166, 09210-170, Santo André, Brazil

(Received 11 August 2008; published 15 October 2008)

We report two-channel calculations for $e^{\pm}$-H_2 scattering ($X^1\Sigma_g^+ \rightarrow X^1\Sigma_g^+, B^3\Sigma_u^+$ for electrons and $X^1\Sigma_g^+ \rightarrow X^1\Sigma_g^+, B^1\Sigma_u^+$ for positrons). We provide independent estimates of the electron $^2\Sigma_g^+$ Feshbach resonance (though for a limited range of interatomic distances) in good agreement with benchmark calculations [D. T. Stibbe and J. Tennyson, J. Phys. B **31**, 815 (1998)]. Resonance enhanced vibrational excitation cross sections were obtained with a time-dependent local complex potential approach and compare favorably with recent calculations [R. Celiberto *et al.*, Phys. Rev. A **77**, 012714 (2008)] and experimental data. The time resolution also provides good physical insight into the transient dynamics. In a previous work, we predicted the existence of a positron-hydrogen $^2\Sigma_g^+$ Feshbach resonance based on a fixed-nuclei scattering calculation (equilibrium geometry) that was not observed experimentally [J. P. Sullivan *et al.*, J. Phys. B **34**, L467 (2001)]. We further investigate the resonance potential in this study and our results indicate that the $^2\Sigma_g^+$ potential crosses the $B^1\Sigma_u^+$ state just above the equilibrium interatomic distance of the ground state, giving rise to a short-lived transient. Though the positronium formation channel could also play a role, the state crossing sheds light on the controversy between theory and experiment.

DOI: 10.1103/PhysRevA.78.042704 PACS number(s): 34.80.Gs, 34.80.Uv, 34.80.Lx

I. INTRODUCTION

The formation of temporary ion states (resonances) in electron scattering by molecules has long been acknowledged [1]. The transients are usually classified as shape resonances when the electron is trapped by the molecular ground state (combination of centrifugal barrier and polarization potential); core-exited shape resonances when the ion state energy lies above an electronically excited parent state; and Feshbach resonances when the (electronically excited) parent state lies above the resonant state. Long-lived resonances efficiently transfer energy into nuclear degrees of freedom, thus giving rise to a variety of electron-driven processes, ranging from the formation of reactive species in cold plasmas [2] to mutagenic DNA strand breaks [3]. One of the most striking differences between electron and positron scattering by molecules is the lack of such resonances in the latter case. Positrons form low-lying virtual [4] and bound states [5,6] that give rise to vibrational resonances, but the repulsive positron-molecule static potentials seem to hinder the formation of shape and (electronic) Feshbach resonances. Though the existence of p-wave e^+-Mg and e^+-Ca shape resonances was recently predicted [7], no experimental evidence of positron-molecule resonances has been provided.

The e^--H_2 complex has well-know resonances in the 11–15 eV range [8,9] related to several singlet and triplet excited electronic states [10,11]. This resonance manifold was resolved into four series, named a–d, by Comer and Read [8]. The most prominent, series a, arises from a $^2\Sigma_g^+$ Feshbach resonance related to several parent excited states [11], though it closely follows the potential energy curve of the $a^3\Sigma_g^+$ state over a fairly broad range of internuclear distances. The complex potential of this $^2\Sigma_g^+$ resonance, among several others, was obtained from R-matrix scattering calculations by Stibbe and Tennyson [11] and recently extrapolated to smaller ($R < 1.1a_0$) and larger ($R > 4.0a_0$) bond lengths by Celiberto *et al.* [12]. This resonance was previously obtained with the Schwinger multichannel method (SMC) at the equilibrium geometry [13], and a similar resonant feature was also observed in positron scattering calculations [14]. Though these calculations, performed at the equilibrium geometry of the target, showed a clear signature of a $^2\Sigma_g^+$ Feshbach resonance, experimental integral cross sections obtained with high resolution positron beams did not observe any resonant feature [15].

In this work, we perform a comparative study of electron and positron multichannel scattering at several bond lengths to access the complex potentials of the $^2\Sigma_g^+$ resonances. The comparison of electron and positron cross sections often provide insight into the underlying physics of matter-antimatter interactions [16,17], and the present study elucidates the reason why no experimental evidence of a e^+-H_2 resonance was found. We also obtain resonantly enhanced vibrational excitation cross sections by electron impact, corresponding to the series a of Comer and Read—in view of the relevance of temporary ions to hydrogen plasmas [18] and the recent applications to nanotechnology [19], we believe the vibrational resolution of the $^2\Sigma_g^+$ resonance has received little attention. Vibrationally resolved cross sections were recently calculated by Celiberto *et al.* [12] with a time-independent local potential approach, employing the benchmark potentials of Stibbe and Tennyson [11] for $1.1a_0 \leqslant R \leqslant 4.0a_0$, and judicious extrapolation schemes for other bond lengths. We obtain independent estimates of the resonance potentials from SMC scattering calculations (over a limited range of internuclear distances), and employ a time-dependent approach that provides further insight into the transient vibration dynamics.

Our theoretical formulation is outlined in Sec. II A and the numerical aspects are discussed in Sec. III. The results of

the comparative study of electron and positron scattering are presented in Sec. IV and our conclusions are given in Sec. V.

II. THEORY

A. Time-dependent local complex potential approach

In the present study we employ a Feshbach projection operator approach [20] to the dynamics of metastable states. Several formulations of the projection operator formalism accounting for nuclear vibrations have been proposed [21–26] and rely on a Born-Oppenheimer [27] electronic discrete state, $\phi_d(\mathbf{R}_N,\mathbf{r}_p;R)$; where $\mathbf{R}_N=(\mathbf{r}_1,\mathbf{r}_2,\cdots,\mathbf{r}_N)$ denotes the coordinates of N target electrons, $\mathbf{r}_p$ the coordinates of the projectile (either an electron or a positron), and R is the internuclear distance. The discrete state defines the projectors $\mathcal{Q}=|\phi_d\rangle\langle\phi_d|$ and $\mathcal{P}=(1-\mathcal{Q})$ that account for the coupling of continuum states ($\mathcal{P}$ space) to the $(N+1)$-particle discrete state describing the trapped projectile ($\mathcal{Q}$ space). Since we closely follow the local complex potential (LCP) formulation of Hazi *et al.* [26], only a few key aspects will be addressed here.

The Schrödinger equation for the collision problem is

$$H|\Psi^{(+)}_{\mathbf{k}_i n_i \nu_i}\rangle = E|\Psi^{(+)}_{\mathbf{k}_i n_i \nu_i}\rangle, \tag{1}$$

where $\mathbf{k}_i$ is the wave vector of the projectile, n_i and ν_i denote the initial electronic and vibrational eigenstates of the target, respectively, and the Hamiltonian is given by

$$H = K + H_{ele} \equiv K + H_0 + V. \tag{2}$$

In the expression above, K is the nuclear kinetic energy operator, V is the projectile-molecule scattering potential, and H_0 is the interaction-free Hamiltonian, i.e., the sum of the projectile kinetic energy and the N-electron target Hamiltonian,

$$H_0 = -\frac{1}{2}\nabla_p^2 + H_N, \tag{3}$$

with the nuclear repulsion included in the latter. The resonance nuclear state is given by

$$|\xi_{d\nu_i}(R)\rangle = \langle\phi_d|\Psi^{(+)}_{\mathbf{k}_i n_i \nu_i}\rangle, \tag{4}$$

where integration over electron (positron) coordinates is implied, and satisfies

$$\left(E - K - E_{res}(R) + \frac{i}{2}\Gamma(R)\right)\xi_{d\nu_i}(R) = \left(\frac{\Gamma_X(R)}{2\pi}\right)^{1/2}\eta_{\nu_i}(R), \tag{5}$$

if a local approximation for the resonant potential is employed. η_{ν_i} is the initial vibrational eigenstate of the target, E_{res} and Γ are the real and imaginary parts of the LCP, and Γ_X is the partial width for capture from (decay into) the ground electronic state (Γ is the total width, given by the sum of the partial widths of all energetically allowed electronic states). In deriving Eq. (5), the main assumption is the weak dependence of the discrete-continuum coupling matrix element [28],

$$U_{\mathbf{k}n\nu}(R) = \langle\phi_d|\mathcal{Q}H_{ele}\mathcal{P}|\Psi^{(+)}_{\mathbf{k}n\nu}\rangle, \tag{6}$$

on both the vibrational quantum number (ν) and projectile energy (E); see Ref. [26] for details. The LCP approximation T matrix element for vibrational excitation is given by

$$T_{\nu_i,\nu_f}(E) = \langle\eta_{\nu_f}|\left(\frac{\Gamma_X}{2\pi}\right)^{1/2}|\xi_{d\nu_i}\rangle. \tag{7}$$

Equation (5) describes the formation of a transient ion that launches a stationary vibrational eigenstate of the target (η_{ν_i}) onto a complex potential surface. Better physical insight is gained by Fourier transforming [29,30] Eqs. (5) and (7),

$$i\frac{\partial}{\partial t}\xi_{d\nu_i}(R,t) = \left(E - K - E_{res}(R) + \frac{i}{2}\Gamma(R)\right)\xi_{d\nu_i}(R,t), \tag{8}$$

for $t>0$, where

$$\xi_{d\nu_i}(R,t\to 0^+) = \left(\frac{\Gamma_X(R)}{2\pi}\right)^{1/2}\eta_{\nu_i}(R) \tag{9}$$

and $\xi_{d\nu_i}(R,t<0)=0$. The vibrational excitation T matrix and integral cross section are given by

$$T_{\nu_i,\nu_f}(E) = -i\int_0^\infty dt e^{iEt}\langle\eta_{\nu_f}|\left(\frac{\Gamma_X}{2\pi}\right)^{1/2}|\xi_{d\nu_i}(t)\rangle \tag{10}$$

and

$$\sigma_{\nu_i,\nu_f}(E) = \frac{4\pi^3}{k_i^2}|T_{\nu_i,\nu_f}(E)|^2, \tag{11}$$

respectively, where k_i is the magnitude of the projectile incident wave vector.

B. Schwinger multichannel method

The resonance complex potential surfaces are obtained from fixed-nuclei *ab initio* calculations performed with the SMC approach. The implementations for electron [31] and positron [32] scattering are discussed in detail elsewhere, and here we only give the working expression for the fixed-nuclei transition matrix,

$$t_{\mathbf{k}_i,\mathbf{k}_f}(E) = \sum_{m,n}\langle S_{\mathbf{k}_f}|V|\chi_m\rangle(d^{-1})_{mn}\langle\chi_n|V|S_{\mathbf{k}_i}\rangle, \tag{12}$$

where

$$d_{mn} = \langle\chi_m|\left[\frac{\hat{H}_{ele}}{(N+1)} - \frac{\hat{H}_{ele}P + P\hat{H}_{ele}}{2} + \frac{VP+PV}{2} - VG_P^{(+)}V\right] \times|\chi_n\rangle \tag{13}$$

for electrons and

$$d_{mn} = \langle\chi_m|(PVP + Q\hat{H}_{ele}Q - VG_P^{(+)}V)|\chi_n\rangle \tag{14}$$

for positrons. In the expressions above, P is a projector onto energy-allowed target electronic channels, $Q=(1-P)$, $G_P^{(+)}$ is the free-particle Green's function projected onto P space, $\hat{H}_{ele}=E-H_{ele}$, and V is the projectile-target interaction potential. The $(N+1)$-particle configuration state functions χ_m are

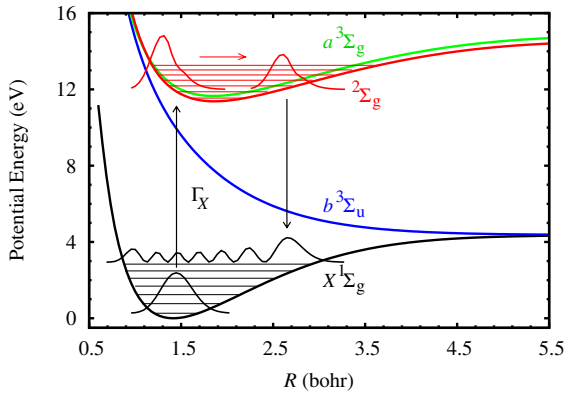

FIG. 1. (Color online) Resonance-assisted vibrational excitation scheme. The $^2\Sigma_g^+$ Feshbach resonance is formed by electron attachment (width Γ_X), thus launching the vibrational eigenstate of the target onto the transient complex potential. The system can decay to a vibrationally excited state of the $X^1\Sigma_g^+$ potential by electron detachment (width Γ_X). Decay to other collision channels is not shown.

given by products of target electronic states and projectile scattering orbitals, and provide the basis for expansion of the trial scattering wave function (the scattering orbital is antisymmetrized to the target orbitals for electron collisions). The open electronic collision channels are included in the P space and the dynamical response of the target electrons to the projectile field (polarization effects) are accounted for through the Q space (virtual excitations of the target).

III. COMPUTATIONAL PROCEDURES

A. Fixed-nuclei calculations

The Cartesian Gaussian basis sets used in fixed-nuclei calculations are given elsewhere for both positron [33,34] and electron [35] scattering. The target electronic ground state was described at the restricted Hartree-Fock (RHF) level and all virtual orbitals were generated with an improved-virtual-orbital (IVO) scheme [36]. The target was treated as a D_{2h} molecule due to limitations of the computer codes. Scattering calculations were performed for several internuclear distances ranging from $R=1.141a_0$ to $R=2.506a_0$. For each R, the projectile energies were taken up to the excitation threshold of the $a^3(E^1)\Sigma_g^+$ state, where the triplet (singlet) state was considered in studies of electron (positron) scattering. The projector P in Eqs. (13) and (14) thus included the $X^1\Sigma_g^+$ and $b^3\Sigma_u^+$ ($E^1\Sigma_u^+$) states, and all singly excited closed target states were taken into account to describe polarization effects.

A Koopmans' theorem estimate of the ionization potential yields the positronium formation threshold $E_{\mathrm{Ps}}=9.38$ eV in our model (equilibrium geometry), lying 0.8 eV above the experimental value, $E_{\mathrm{Ps}}=8.6$eV. Though the positronium formation channel should be open in the energy range addressed in positron collisions, it is not included in our model due to limitations of the current SMC implementation.

B. Vibrational excitation calculations

The operators and vibrational wave packet in Eq. (8) were represented on an evenly spaced 1024-point grid ranging from $0.6a_0$ to $12.0a_0$. The time-evolution operator was described with the split-operator scheme [37] combined with a fast Fourier transform (FFT) algorithm for the kinetic energy operator [38]. The time-energy Fourier transform in Eq. (10) was carried out with a 262 144-point FFT and upper integration limit $t_{\max}=3$ ps; this was more than enough to assure convergence since results obtained with a 65 536-point time grid and $t_{\max}=750$ fs were essentially identical. The target vibrational eigenstates were obtained from the benchmark $X^1\Sigma_g^+$ potential energy curve of Kolos and Wolniewicz [39] employing the energy screening technique [40] (the eigenstates were also represented on the numerical grid described above).

IV. RESULTS AND DISCUSSION

A. Electron scattering

The resonance-assisted vibrational excitation is schematically shown in Fig. 1. Though the neutral potential surfaces

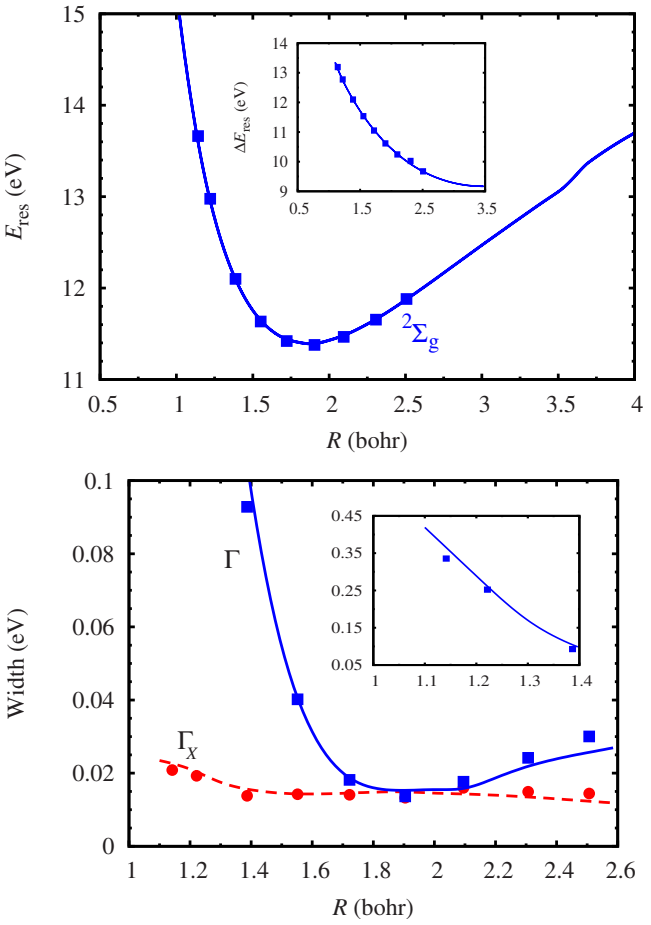

FIG. 2. (Color online) Upper panel: real part (E_{res}) of the $^2\Sigma_g^+$ complex potential. The squares are present results and the lines are obtained from cubic-spline interpolation of the potential of Ref. [11]. The inset shows the resonance positions (ΔE_{res}) obtained from scattering calculations. Lower panel: imaginary part of the $^2\Sigma_g^+$ complex potential. The blue (solid) and red (dashed) lines are the total (Γ) and partial (Γ_X) widths of Ref. [11], respectively (also obtained from cubic-spline interpolation). The squares and circles are present results for Γ and Γ_X, respectively. The inset shows the total width at small internuclear distances.

may be taken from benchmark calculations [39] or generated with quantum chemistry codes, the $^2\Sigma_g^+$ complex potential should in principle be obtained from scattering calculations. One of the limitations of the current SMC implementation is the lack of target correlation, described at the RHF level of approximation. The quality of RHF potentials rapidly deteriorates as the molecule is displaced from the equilibrium geometry, thus hindering fixed-nuclei scattering calculations far off the Frank-Condon region of the vibrational ground state. Nevertheless, resonance energies ($E_{\rm res}$) are relative to the target ground state potential (E_X),

$$E_{\rm res}(R) = E_X(R) + \Delta E_{\rm res}(R), \tag{15}$$

where $\Delta E_{\rm res}$ is the resonance position obtained from scattering calculations. Since the resonance position will be faithfully described as long as correlation-polarization effects in the neutral target and transient ion are balanced with respect to each other, accurate resonance potentials may be obtained from SMC calculations with the help of a correlated ground state potential,

$$E_{\rm res}(R) = E_X^{\rm KW}(R) + \Delta E_{\rm res}^{\rm SMC}(R), \tag{16}$$

where $\Delta E_{\rm res}^{\rm SMC}(R)$ is obtained from SMC scattering calculations (RHF target) and $E_X^{\rm KW}(R)$ is the $X^1\Sigma_g^+$ potential of Kolos and Wolniewicz [39].

Resonance positions and total widths (Γ) were obtained from least-squares fits of Breit-Wigner profiles [41] to scattering cross sections (the background was described with second degree polynomials, though an essentially linear dependence on energy was always observed). The resonance potential obtained from the least-squares fits and Eq. (16) is shown in the upper panel of Fig. 2 (squares), along with the results of Ref. [11], obtained with a thorough description of target correlation. The very good agreement suggests that SMC calculations provide a faithful description of the resonance potential, though over a limited range of internuclear distances, despite the lack of target correlation. The widths are compared with those of Stibbe and Tennyson [11] in the lower panel of Fig. 2. The present partial width (Γ_X) was estimated with the help of the branching ratios given in Ref. [11], though it could in principle be obtained from the T matrix [42]. Our results favorably compare with the benchmark calculations, though some discrepancies are seen for the outermost points (see also Table I).

TABLE I. Resonance positions and widths. The results of Stibbe and Tennyson [11] were interpolated with cubic splines.

	$\Delta E_{\rm res}$ (eV)		Γ (meV)	
R (bohr)	Present	Ref. [11]	Present	Ref. [11]
1.141	13.192	13.132	335	367
1.221	12.774	12.755	252	261
1.387	12.097	12.094	92.8	104
1.552	11.536	11.550	40.2	40.6
1.722	11.051	11.072	18.1	18.7
1.904	10.617	10.557	13.6	15.3
2.095	10.244	10.261	11.8	15.8
2.307	10.024	9.921	2.42	2.19
2.507	9.673	9.669	3.00	2.57

Celiberto *et al.* [12] recently surveyed the sensitivity of vibrational excitation cross sections with respect to small

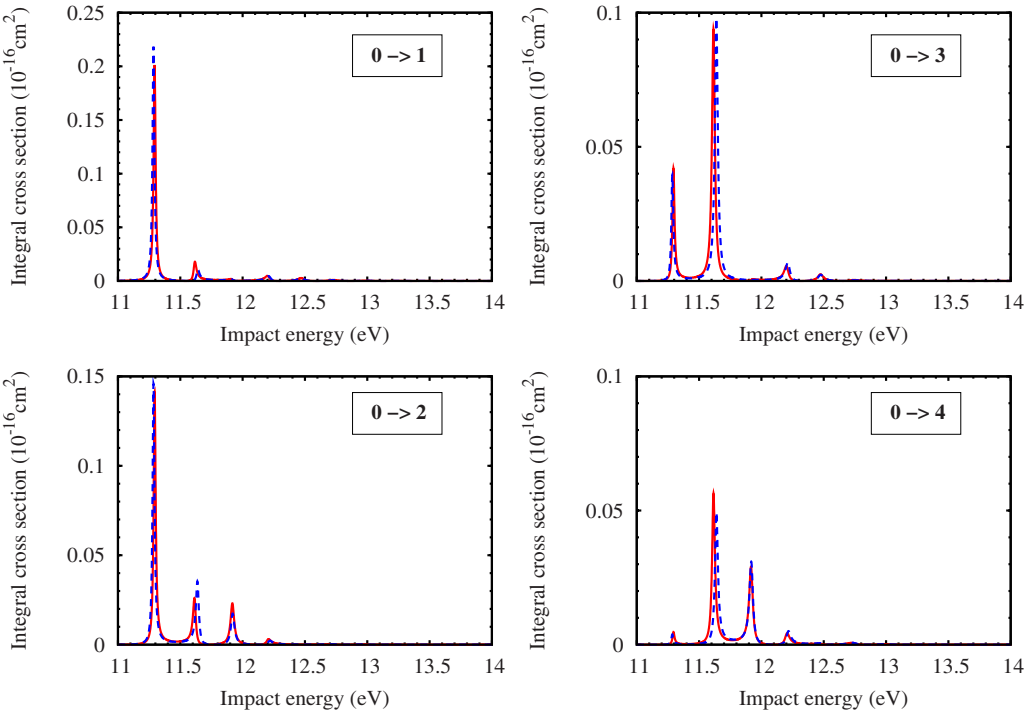

FIG. 3. (Color online) Vibrational excitation cross sections calculated with the resonance potential of Refs. [11,12] (solid red lines) and with a potential that incorporates SMC estimates over a limited range of internuclear distances (dashed blue lines); see text for details.

TABLE II. Resonance spectra ($\epsilon_\nu^{\rm res}$), squared Frank-Condon overlaps ($|\langle \eta_0 | \eta_\nu^{\rm res}\rangle|^2$), and transition amplitudes ($\langle \eta_0|\Gamma_X|\eta_\nu^{\rm res}\rangle$, $\langle \eta_0|\Gamma|\eta_\nu^{\rm res}\rangle$) obtained from the resonance potential of Refs. [11,12] (*benchmark*) and from a potential that incorporates SMC estimates over a limited range of internuclear distances (*present*). All values (both *present* and *benchmark*) were obtained from the complex potential surfaces employing numerical the procedures described in Sec. III.

	$\epsilon_\nu^{\rm res}$ (eV)		$\|\langle \eta_0 \| \eta_\nu^{\rm res}\rangle\|^2$		$\langle \eta_0\|\Gamma_X\|\eta_\nu^{\rm res}\rangle$ (meV)		$\langle \eta_0\|\Gamma\|\eta_\nu^{\rm res}\rangle$ (meV)	
ν	Present	benchmark	Present	benchmark	Present	benchmark	Present	benchmark
0	11.283	11.292	0.2258	0.2110	6.699	6.793	18.11	18.95
1	11.637	11.614	0.2566	0.2545	7.210	7.570	28.92	30.21
2	11.918	11.916	0.1815	0.2009	6.193	6.889	34.03	38.53
3	12.212	12.202	0.1330	0.1316	5.489	5.802	41.19	43.47
4	12.473	12.472	0.0835	0.0807	4.542	4.812	43.89	45.87
5	12.731	12.728	0.0480	0.0487	3.651	4.021	44.02	46.45
6	12.979	12.977	0.0294	0.0294	3.088	3.407	44.45	45.88
7	13.225	13.223	0.0169	0.0174	2.589	2.879	42.63	43.87
8	13.454	13.452	0.0086	0.0091	2.081	2.287	37.36	38.30
9	13.631	13.628	0.0044	0.0047	1.654	1.766	30.99	31.45

($\sim$10%) variations of the resonance potential. Though their results were essentially insensitive to different extrapolation schemes, significant change arised from variations of the potential shape for $1.1a_0 \leqslant R \leqslant 4.0a_0$. It would thus be interesting to check the impact of the small discrepancies seen in Fig. 2 on vibrationally resolved cross sections. We employed the time-dependent LCP approach described above for (i) the resonance potential of Ref. [12], obtained from judicious extrapolation of the potential of Stibbe and Tennyson [11]; and (ii) a modified potential obtained from the present SMC calculations for $1.14a_0 \leqslant R \leqslant 2.50a_0$, and the potential of Ref. [12] otherwise (see Fig. 3). The peak positions are essentially identical, reflecting the agreement between the resonance spectra (eigenvalues of $E_{\rm res}$), though the slightly discrepant peak heights are mostly due to the widths. This can be observed in Table II, where the real parts of the resonance potentials are compared through the spectra ($\epsilon_\nu^{\rm res}$) and the Frank-Condon intensities $|\langle \eta_0 | \eta_\nu^{\rm res}\rangle|^2$, while the imaginary parts are compared through the amplitudes $\langle \eta_0|\Gamma_X|\eta_\nu^{\rm res}\rangle$ and $\langle \eta_0|\Gamma|\eta_\nu^{\rm res}\rangle$, where $|\eta_\nu^{\rm res}\rangle$ is an eigenstate of $E_{\rm res}$, and $|\eta_0\rangle$ is the $\nu=0$ level of the target $X^1\Sigma_g^+$ potential. Though the Frank-Condon overlaps may also contribute to discrepancies in the peak heights, the transition amplitudes clearly show larger deviations than the resonance spectra.

In Figs. 4–6 we compare calculated differential cross sections (DCS) at 85° with the experimental data of Comer and Read [8] and the calculations of Celiberto *et al.* [12]. The present results were obtained with the resonance potential that incorporates SMC calculations over a limited range of internuclear distances [potential (ii) described above]. On the assumption that angular distributions are weakly coupled to vibrations, DCS can be obtained by applying the angular factor

$$g_2(\theta) = \frac{15}{14}\left[\frac{1}{4\pi}(1 - 2\cos^2\theta + 3\cos^4\theta)\right] \tag{17}$$

to Eq. (11), where a dominant d wave contribution has been assumed, according to the analysis of Joyez *et al.* [9]. The calculated DCS were also convoluted over a Lorentzian profile with full width at half maximum $\Gamma=40$ meV to account for the experimental resolution [8]. The disagreement between theory and experiment for the $0\rightarrow1,2$ excitations is due to the neglect of background scattering in both calculations (the minima in the experimental DCS indicates a large background for the $0\rightarrow1$ DCS that rapidly vanishes for higher transitions). For excitation to the lower ($0\rightarrow2,3,4,5$) excited states, the present calculations show a somewhat better agreement with the experimental data than those of Celiberto *et al.* [12], since the heights of the peaks related to the $\nu_{\rm res}=0,1,2$ resonance states are better described (subtracting the background contribution). For higher excitations ($0\rightarrow7,8,9$) our results are underestimated and the calculations of Ref. [12] compare more favorably with experiment. It is not easy to infer the underlying reasons for the discrepancies between the calculations, though they would be expected to arise from the numerical frameworks (in addition to small differences in the resonance potentials).

To survey the time evolution of the vibrational wave packet on the resonance potential, we define the survival probability

$$S_{\rm prob}(t) = \frac{\langle \xi_{{\rm d}\nu_i}(t)|\xi_{{\rm d}\nu_i}(t)\rangle}{\langle \xi_{{\rm d}\nu_i}(t=0)|\xi_{{\rm d}\nu_i}(t=0)\rangle} \equiv \frac{1}{\langle \xi_{{\rm d}\nu_i}(t=0)|\xi_{{\rm d}\nu_i}(t=0)\rangle} s(t), \tag{18}$$

normalized to unit at $t=0$ for convenience, and the position expectation value

$$\langle R\rangle(t) = \frac{1}{s(t)}\langle \xi_{{\rm d}\nu_i}(t)|R|\xi_{{\rm d}\nu_i}(t)\rangle. \tag{19}$$

These quantities are shown in Fig. 7, where a fast decay of the survival probability is observed (an exponential function

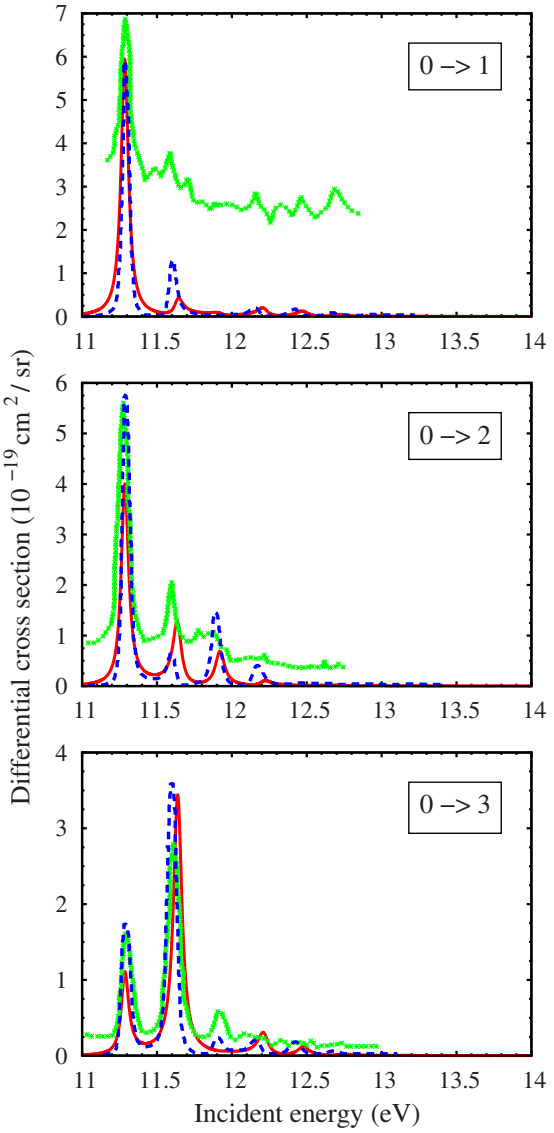

FIG. 4. (Color online) Vibrational excitation differential cross section at 85°. Red solid lines: present results; blue dashed lines: calculations of Celiberto *et al.* [12]; green stars: experimental data of Ref. [8].

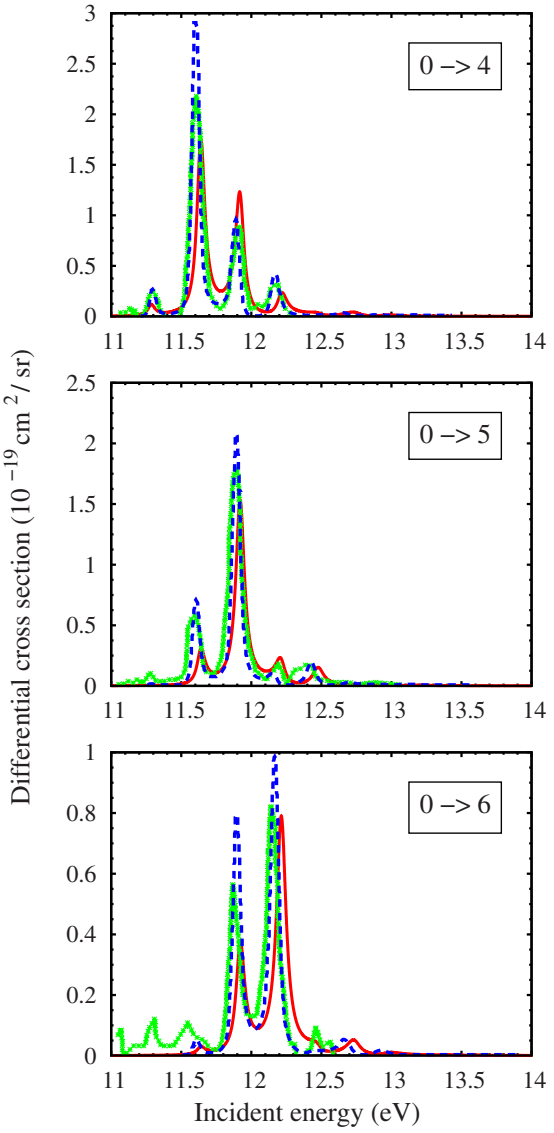

FIG. 5. (Color online) Same as in Fig. 4.

with $\alpha=0.045$ fs^{-1} is a reasonable approximation for S_{prob}). The position expectation value oscillates in the basin of the real part of the resonance potential, as expected. Though not shown here, $\langle R\rangle$ subsequently tends to higher values, reaching 5 bohr around 250 fs. This would suggest that dissociative attachment could take place from tunneling through the resonance barrier, but the survival probability becomes negligible for relatively short times ($S_{\text{prob}}\sim 0.0004$ for $t=250$ fs).

Snapshots of the vibrational wave packet probability are shown in Fig. 8 (normalized to unit at $t=0$ for the sake of presentation). The wave packet is initially nearly Gaussian shaped (upper panel), but rapidly becomes more complicated as it bounces off the outer classical turning point, around $t=7$ fs. The plots in the central and lower panels indicate that the oscillations of the position expectation value (Fig. 7) do not arise from reflections of a bell-shaped wave packet, but from complex interference effects. The relative heights of innermost and outermost probability peaks give rise to the successive minima and maxima of $\langle R\rangle$, though a revival of a Gaussian-like shape is seen around 50–60 fs (lower panel).

B. Positron scattering

Apart from the inherent differences between the description of electron and positron collisions, our methodology to study positron-H_2 scattering is essentially the same employed for electrons. Fixed-nuclei SMC calculations were carried out for several interatomic distances, within a limited range due to the lack of target correlation, and for energies up to the excitation threshold of the $E^1\Sigma_g^+$ state, where the $X^1\Sigma_g^+\rightarrow B\ ^1\Sigma_u^+$ excitation was taken into account above the threshold. The fixed-nuclei data are summarized in Fig. 9, where the A_g-symmetry partial integral cross section (ICS) is shown for electrons (upper panel, $X^1\Sigma_g^+\rightarrow b\ ^3\Sigma_u^+$) and positrons (lower panel, $X^1\Sigma_g^+\rightarrow X\ ^1\Sigma_g^+$ plus $X^1\Sigma_g^+\rightarrow B\ ^1\Sigma_u^+$) for

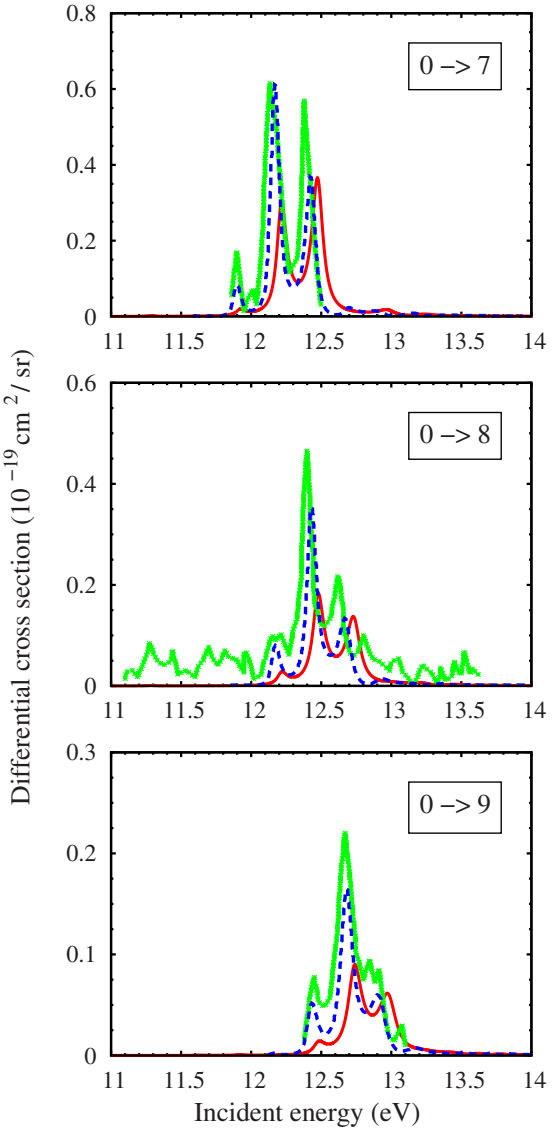

FIG. 6. (Color online) Same as in Fig. 4.

selected bond lengths. At the equilibrium geometry (R_{eq}), a sharp resonant structure is seen in both calculations, below the thresholds of the $a^3\Sigma_g^+$ and $B^1\Sigma_u^+$ states for electrons and positrons, respectively. As discussed elsewhere [14], the square-integrable trial basis set employed in SMC calculations provides a representation for the e^+-H_2 Hamiltonian, and the pseudoeigenstates obtained from diagonalization of this matrix support the interpretation of the narrow ICS peak as a Feshbach resonance arising from an admixture of $B^1\Sigma_u^+$ and $E^1\Sigma_g^+$ parent states. Despite the similarity between the resonant structures observed in electron and positron scattering calculations at the equilibrium bond length, existence of the positron resonance was not supported by high resolution experiments [15]. The present results shed light on this controversy since the e^+-H_2 resonance peak disappears as the molecule is stretched, while it is present in all electron scattering calculations.

To understand the underlying physics of Fig. 9 we built up the potential curve of the positron resonance. Since the calculated cross sections are rather flat for the stretched geometries, fits of Breit-Wigner profiles would not be meaningful. To overcome this difficulty, estimates of the real part of the resonance potential were obtained from the pseudospectrum of the positron-molecule compound. Whenever a clear resonant peak was present, one pseudoeigenvalue was always very close to the resonance peak energy (10^{-3} eV deviations) and the corresponding eigenvector was always essentially given by an admixture of $B^1\Sigma_u^+$ and $E^1\Sigma_g^+$ parent states. This composition of the pseudoeigenvector was observed even for the larger interatomic distances having nonresonant cross sections, and thus provided a convenient procedure to obtain the positron resonance potential (the consistency of this procedure was also checked by closing the $B^1\Sigma_u^+$ channel to give rise to spurious resonance peaks). The real part of this resonance potential is shown in Fig. 10 along with the relevant excited singlet states. The $^2\Sigma_g^+$ potential crosses the $B^1\Sigma_u^+$ curve slightly above the equilibrium position of the ground state (R_{eq}), close to the center of the Frank-Condon region. As a result, the Feshbach resonance obtained for $R \lesssim R_{eq}$ rapidly changes into a core-excited shape resonance that readily decays to the $B^1\Sigma_u^+$ channel, thus giving rise to flat cross sections for stretched geometries (lower panel of Fig. 9)—the electron $^2\Sigma_g^+$ potential, on the other hand, lies slightly below the $a^3\Sigma_g^+$ state over a broad range of interatomic distances, thus keeping the Feshbach character. The imaginary part of the positron $^2\Sigma_g^+$ potential could be obtained for the equilibrium geometry ($\Gamma = 7.89$ meV) and shorter bond

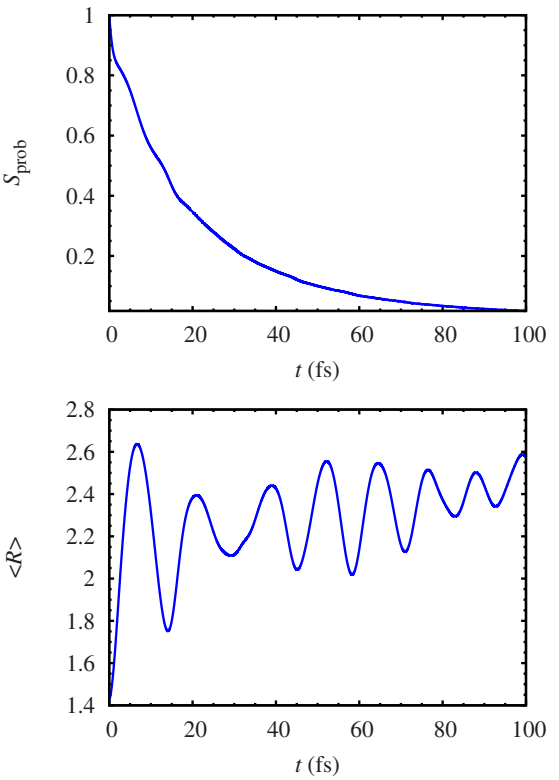

FIG. 7. (Color online) Time evolution of the vibrational wave packet on the resonance state. The upper panel shows the survival probability normalized to unit at $t=0$, as defined in Eq. (18). The position expectation value is shown in the lower panel in units of Bohr radius.

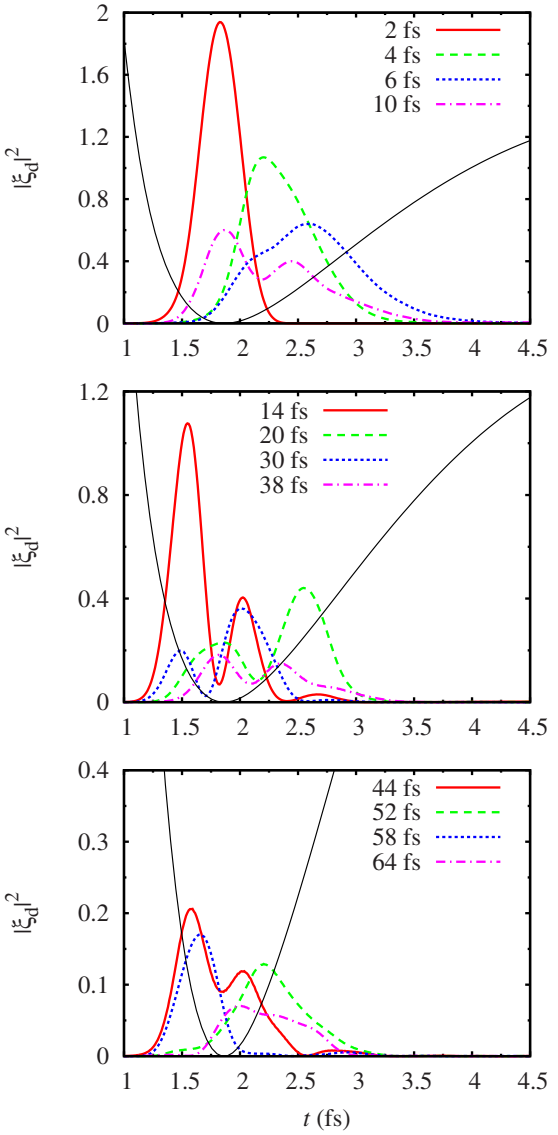

FIG. 8. (Color online) Snapshots of the wave packet probability on the resonance state, normalized to unit at $t=0$ for convenience. The real part of the resonance potential is also indicated (thin solid line). The plots in the central and lower panel correspond to selected maxima and minima of the position expectation value (Fig. 7). Minima: $t=14$ fs, 30 fs, 44 fs, and 58 fs. Maxima: $t=20$ fs, 38 fs, 52 fs, and 64 fs.

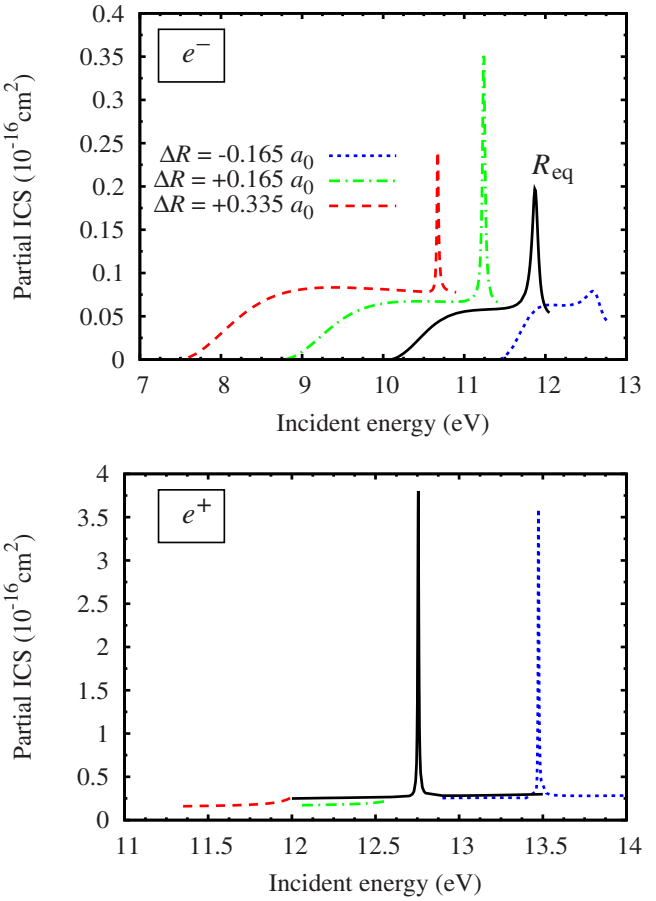

FIG. 9. (Color online) A_g-symmetry partial integral cross sections. Upper panel: electron-impact $X^1\Sigma_g^+ \rightarrow b^3\Sigma_g^+$ excitation; lower panel: sum of positron-impact elastic ($X^1\Sigma_g^+ \rightarrow X^1\Sigma_g^+$) and $X^1\Sigma_g^+ \rightarrow B^1\Sigma_u^+$ excitation. Both panels show calculations for the ground state equilibrium interatomic distance (R_{eq}) and selected displaced geometries $\Delta R=(R-R_{eq})$, as indicated in the upper panel (units of Bohr radius). For each bond length, calculations were performed for energies up to the threshold of the $a^3\Sigma_g^+$ state (electrons) and $E^1\Sigma_g^+$ state (positrons).

lengths, $\Delta R=-0.165a_0$ ($\Gamma=6.02$ meV) and $\Delta R=-0.335a_0$ ($\Gamma=5.41$ meV), but not for stretched geometries since least-squares fits of Breit-Wigner profiles to flat cross sections would not be meaningful.

Though the potential curves could be affected by an improved description of target correlation, we believe the crossing between the $^2\Sigma_g^+$ and $B^1\Sigma_u^+$ potentials would still take place, and our conclusions would still hold (the same procedure accurately described the dynamics of electron collisions). The absence of resonance fingerprints in the experimental cross sections can therefore be understood. Assuming vertical positron attachment, the wave packet would spread over the region where the resonance width changes from very narrow ($R<R_{eq}$) to very broad ($R>R_{eq}$), so the average width over the Frank-Condon region would be large. In addition, the potential slope would push the wave packet towards larger bond lengths in a very short time (see the electron resonance case, Fig. 8) so the $R<R_{eq}$ region would hardly affect the dynamics. Though the Born-Oppenheimer Feshbach resonance is formally predicted for $R \lesssim R_{eq}$, it would have a very short lifetime and hence no experimental signature.

Finally, we mention that our calculations do not take the positronium formation channel into account. Though this additional decay channel would in principle broaden any resonance state, it would not be expected to significantly affect the state-crossing dynamical picture discussed above (the width for $R \lesssim R_{eq}$ could be increased, though). We also observe that similar fixed-nuclei SMC calculations compare favorably with the experimental $X^1\Sigma_g^+ \rightarrow B^1\Sigma_g^+$ excitation cross section [43] despite the significant magnitude of the positronium formation cross section [44].

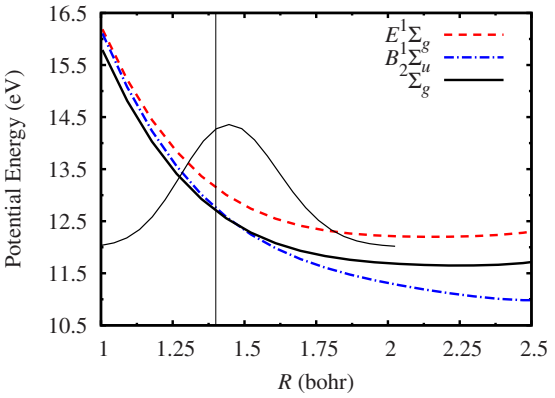

FIG. 10. (Color online) Potential energy curves for the hydrogen molecule ($B^1\Sigma_g^+$ and $E^1\Sigma_g^+$ states) and the e^+-H_2 compound ($^2\Sigma_g^+$). The vertical line indicates the equilibrium position of the hydrogen ground state ($X^1\Sigma_g^+$) and the thin solid line indicates the probability of its $\nu=0$ vibrational level (Frank-Condon region).

V. CONCLUSIONS

We performed two-channel calculations for electron and positron scattering by hydrogen molecules. For electrons, we provided independent estimates of the $^2\Sigma_g^+$ resonance potential, though for a limited range of interatomic distances due to the lack of target correlation, described at the RHF level. Despite this limitation, we obtained good agreement with the benchmark calculations of Stibbe and Tennyson [11] combining SMC estimates of resonance positions with a correlated potential for the target ground state. With the help of a judicious extrapolation scheme proposed by Celiberto *et al.* [12], we could vibrationally resolve the cross sections employing a time-dependent local complex potential approach. Our cross sections compared favorably to experimental data [8] and to the time-independent calculations of Ref. [12]. Snapshots of the vibrational wave packet revealed a rich transient dynamics.

The real part of the positron-hydrogen $^2\Sigma_g^+$ potential was also obtained from SMC calculations. For small bond lengths ($R \lesssim R_{\mathrm{eq}}$) it has a Feshbach character that lead us to incorrectly predict that a Feshbach resonance could be observed for this system [14]. The present results indicated that the $^2\Sigma_g^+$ potential crosses the $B^1\Sigma_u^+$ state just above the equilibrium interatomic distance of the ground state, giving rise to a short-lived transient. Though the positronium formation channel could also contribute to broaden the resonance, we believe the state crossing is essential to understand why resonant fingerprints were not observed in high resolution experiments [6].

ACKNOWLEDGMENTS

E.M.O. acknowledges financial support from Coordenação de Aperfeiçoamento de Pessoal de Nível Superior (CAPES), and M.A.P.L. acknowledges support from Conselho Nacional de Desenvolvimento Científico e Tecnológico (CNPq).

[1] G. J. Schulz, Rev. Mod. Phys. **45**, 423 (1973).
[2] A. Grill, *Cold Plasma Materials Fabrication: From Fundamentals to Applications* (IEEE Press, New York, 1994).
[3] B. Boudaïffa, P. Cloutier, D. Hunting, M. A. Huels, and Léon Sanche, Science **287**, 1658 (2000); X. Pan, P. Cloutier, D. Hunting, and L. Sanche, Phys. Rev. Lett. **90**, 208102 (2003).
[4] C. R. C. de Carvalho, Marcio T. do N. Varella, M. A. P. Lima, and E. P. da Silva, Phys. Rev. A **68**, 062706 (2003); M. T. do N. Varella, E. M. de Oliveira, and M. A. P. Lima, Nucl. Instrum. Methods Phys. Res. B **266**, 435 (2008).
[5] G. F. Gribakin, Nucl. Instrum. Methods Phys. Res. B **192**, 26 (2002); G. F. Gribakin and C. M. R. Lee, Phys. Rev. Lett. **97**, 193201 (2006).
[6] S. J. Gilbert, L. D. Barnes, J. P. Sullivan, and C. M. Surko, Phys. Rev. Lett. **88**, 043201 (2002); L. D. Barnes, S. J. Gilbert, and C. M. Surko, Phys. Rev. A **67**, 032706 (2003).
[7] M. W. J. Bromley and J. Mitroy, Phys. Rev. Lett. **97**, 183402 (2006); J. Mitroy and M. W. J. Bromley, *ibid.* **98**, 173001 (2007).
[8] J. Comer and F. H. Read, J. Phys. B **4**, 368 (1971).
[9] G. Joyez, J. Comer, and F. H. Read, J. Phys. B **6**, 2427 (1973).
[10] D. T. Stibbe and J. Tennyson, Phys. Rev. Lett. **79**, 4116 (1997); , J. Phys. B **30**, L301 (1997).
[11] D. T. Stibbe and J. Tennyson, J. Phys. B **31**, 815 (1998).
[12] R. Celiberto, R. K. Janev, J. M. Wadehra, and A. Laricchiuta, Phys. Rev. A **77**, 012714 (2008).
[13] A. J. R. da Silva, M. A. P. Lima, L. M. Brescansin, and V. McKoy, Phys. Rev. A **41**, 2903 (1990).
[14] M. T. do N. Varella, C. R. C. de Carvalho, and M. A. P. Lima, in *New Directions in Antimatter Chemistry and Physics*, edited by C. M. Surko and F. A. Gianturco (Kluwer, Amsterdam, 2001).
[15] J. P. Sullivan, S. J. Gilbert, S. J. Buckman, and C. M. Surko, J. Phys. B **34**, L467 (2001).
[16] F. Arretche, R. F. da Costa, S. d'A. Sanchez, A. N. S. Hisi, E. M. de Oliveira, M. T. do N. Varella, and M. A. P. Lima, Nucl. Instrum. Methods Phys. Res. B **247**, 13 (2006).
[17] J. P. Marler and C. M. Surko, Phys. Rev. A **72**, 062702 (2005).
[18] M. Capitelli and C. Gorse, IEEE Trans. Plasma Sci. **33**, 1832 (2005).
[19] B. N. Khare, M. Meyyappan, A. M. Cassell, C. V. Nguyen, and J. Han, Nano Lett. **2**, 73 (2002); G. Zheng, Q. Li, K. Jiang, X. Zhang, J. Chen, Z. Ren, and S. Fan, *ibid.* **7**, 1622 (2007).
[20] H. Feshbach, Ann. Phys. (N.Y.) **5**, 357 (1958); Ann. Phys. (N.Y.) **19**, 287 (1962).
[21] J. C. Y. Chen, Phys. Rev. **148**, 66 (1966).
[22] T. F. O'Malley, Phys. Rev. **150**, 14 (1966).
[23] J. N. Bardsley, A. Herzenberg, and F. Mandl, Proc. Phys. Soc. London **89**, 321 (1966); J. N. Bardsley, J. Phys. B **1**, 349 (1968).
[24] L. Dubé and A. Herzenberg, Phys. Rev. A **20**, 194 (1979).
[25] W. Domcke and L. S. Cederbaum, Phys. Rev. A **16**, 1465

(1977).
[26] A. U. Hazi, T. N. Rescigno, and M. Kurilla, Phys. Rev. A **23**, 1089 (1981).
[27] M. Born and J. R. Oppenheimer, Ann. Phys. **84**, 457 (1927).
[28] The widths are related to the angle-averaged coupling matrix elements according to

$$\Gamma_n(E-\epsilon_\nu,R,R') = 2\pi U_{E\nu n}(R)U^*_{E\nu m}(R') \simeq 2\pi|U_{E_{\rm res}n}(R)|^2,$$

where ϵ_ν is the energy of the νth vibrational eigenstate. In obtaining the local form (last step above), ϵ_ν is viewed as negligible with respect to the projectile energy (E), and the width is evaluated at the center of the resonance, $\Gamma_n(E,R) \simeq \Gamma_n(E_{\rm res},R)$.
[29] D. T. Birtwistle and A. Herzenberg, J. Phys. B **4**, 53 (1971).
[30] C. W. McCurdy and J. L. Turner, J. Chem. Phys. **78**, 6773 (1983).
[31] K. Takatsuka and V. McKoy, Phys. Rev. A **30**, 1734 (1984); M. A. P. Lima and V. McKoy, *ibid.* **38**, 501 (1988).
[32] J. S. E. Germano and M. A. P. Lima, Phys. Rev. A **47**, 3976 (1993).
[33] J. L. S. Lino, J. S. E. Germano, E. P. da Silva, and M. A. P. Lima, Phys. Rev. A **58**, 3502 (1998).
[34] Marcio T. do N. Varella and M. A. P. Lima, Phys. Rev. A **76**, 052701 (2007).
[35] T. L. Gibson, M. A. P. Lima, V. McKoy, and W. M. Huo, Phys. Rev. A **35**, 2473 (1987).
[36] W. J. Hunt and A. Goddart III, Chem. Phys. Lett. **3**, 414 (1969).
[37] K. Takahashi and K. Ikeda, J. Chem. Phys. **99**, 8680 (1993).
[38] D. Kosloff and R. Kosloff, J. Comput. Phys. **52**, 35 (1983); R. Kosloff, J. Phys. Chem. **92**, 2087 (1988).
[39] W. Kolos and L. Wolniewicz, J. Chem. Phys. **43**, 2429 (1965); W. Kolos and J. Rychlewski, J. Mol. Spectrosc. **169**, 341 (1995).
[40] K. Takatsuka and N. Hashimoto, J. Chem. Phys. **103**, 6057 (1995).
[41] G. Breit and E. P. Wigner, Phys. Rev. **49**, 519 (1936).
[42] A. E. Orel, K. C. Kulander, and T. N. Rescigno, Phys. Rev. Lett. **74**, 4807 (1995); D. J. Haxton, C. W. McCurdy, and T. N. Rescigno, Phys. Rev. A **73**, 062724 (2006).
[43] J. P. Sullivan, J. P. Marler, S. J. Gilbert, S. J. Buckman, and C. M. Surko, Phys. Rev. Lett. **87**, 073201 (2001).
[44] S. Zhou, H. Li, W. E. Kauppila, C. K. Kwan, and T. S. Stein, Phys. Rev. A **55**, 361 (1997); C. K. Kwan, W. E. Kauppila, S. Nazaran, D. Przybyla, N. Scahill, and T. S. Stein, Nucl. Instrum. Methods Phys. Res. B **143**, 61 (1998).